

## A random phased array device for delivery of high intensity focused ultrasound

J W Hand<sup>1,2,6</sup>, A Shaw<sup>3</sup>, N Sathoo<sup>3</sup>, S Rajagopal<sup>3</sup>, R J Dickinson<sup>4</sup>  
and L R Gavrilo<sup>5</sup>

<sup>1</sup> Radiological Sciences Unit, Imperial College Healthcare NHS Trust, Hammersmith Hospital, London W12 0HS, UK

<sup>2</sup> Imaging Sciences Department, Imperial College London (Hammersmith Campus), London W12 0NN, UK

<sup>3</sup> Acoustics Group, National Physical Laboratory, Teddington TW11 0LW, UK

<sup>4</sup> Department of Bioengineering, Imperial College London, London SW7 2AZ, UK

<sup>5</sup> N.N. Andreev Acoustics Institute, 117036 Moscow, Russia

E-mail: [j.hand@imperial.ac.uk](mailto:j.hand@imperial.ac.uk)

Received 9 April 2009, in final form 3 July 2009

Published 1 September 2009

Online at [stacks.iop.org/PMB/54/5675](http://stacks.iop.org/PMB/54/5675)

### Abstract

Randomized phased arrays can offer electronic steering of a single focus and simultaneous multiple foci concomitant with low levels of secondary maxima and are potentially useful as sources of high intensity focused ultrasound (HIFU). This work describes laboratory testing of a 1 MHz random phased array consisting of 254 elements on a spherical shell of radius of curvature 130 mm and diameter 170 mm. Acoustic output power and efficiency are measured for a range of input electrical powers, and field distributions for various single- and multiple-focus conditions are evaluated by a novel technique using an infrared camera to provide rapid imaging of temperature changes on the surface of an absorbing target. Experimental results show that the array can steer a single focus laterally to at least  $\pm 15$  mm off axis and axially to more than  $\pm 15$  mm from the centre of curvature of the array and patterns of four and five simultaneous foci  $\pm 10$  mm laterally and axially whilst maintaining low intensity levels in secondary maxima away from the targeted area in good agreement with linear theoretical predictions. Experiments in which pork meat was thermally ablated indicate that contiguous lesions several  $\text{cm}^3$  in volume can be produced using the patterns of multiple foci.

(Some figures in this article are in colour only in the electronic version)

<sup>6</sup> Author to whom any correspondence should be addressed.

## 1. Introduction

High intensity focused ultrasound (HIFU), an ablative therapy that is unique in having the potential for non-invasive delivery, is currently the subject of considerable research and development (Dubinsky *et al* 2008, ter Haar and Coussios 2007). Although HIFU systems based on the use of a single focused transducer have the advantage of being relatively simple, they have disadvantages, including the need to scan the small focus through clinically relevant volumes of tissue by mechanically translating the transducer. This is time consuming and can lead to clinical treatments of impractically long duration.

The use of phased arrays offers not only electronically controlled dynamic focusing and the ability to vary and control precisely the range, location and size of a focus during treatment without moving the array, but also a means of synthesizing fields with multiple simultaneous foci. Several investigators have proposed phased arrays in which elements are placed on a spherical shell, thereby combining electronic and geometric focusing (Ebbini and Cain 1991, Goss *et al* 1996, Daum and Hynynen 1999, Gavrilov and Hand 2000a). The disadvantages of phased arrays include the unwanted presence of grating lobes and other secondary intensity maxima and, particularly for relatively large extracorporeal 2D arrays, complexity and potentially relatively high cost. There is a common need to reduce grating lobes, and several techniques aimed at achieving this have been reported. Hutchinson *et al* (1996) developed an aperiodic linear array based on a random distribution of different sized elements. Goss *et al* (1996) showed theoretically that the use of elements randomly distributed on a segment of a spherical surface may improve phased array performance. They also suggested that the use of sparse phased arrays may be promising in the reduction of the complexity and relatively high cost of large 2D arrays. Lu *et al* (2005) described the use of a genetic algorithm to optimize the phase and amplitude distributions at array elements to reduce grating lobes. Apodization, broad banding (Dupenloup *et al* 1996) and the use of subsets of elements (Gavrilov *et al* 1997) have also been investigated.

In this work we report details of the initial testing of a phased array comprising elements that are randomly distributed on a segment of a spherical surface according to previous theoretically based criteria (Gavrilov and Hand 2000a, Hand and Gavrilov 2000, 2002). Details of the array's power handling capability, assessment of intensity distributions for both single and multiple foci located at, and displaced axially and laterally from, the geometrical centre of curvature of the spherical segment and the results of tissue ablation in pork meat samples are discussed.

## 2. Materials and methods

### 2.1. The array transducer

The array transducer consisted of 254 circular elements, each 7 mm in diameter, distributed randomly, but with a minimum inter-element (centre to centre) spacing of 7.9 mm, on a spherical surface with a radius of curvature of 130 mm and a diameter of 170 mm. The largest spacing between neighbouring elements was 9.4 mm. The device was constructed using a composite material (Imasonic, Voray sur l'Ognon, France) and was compliant with design criteria described previously (Hand and Gavrilov 2000, Gavrilov and Hand 2000a). A biocompatible epoxy-resin-based matching layer was incorporated at the array surface to improve transmission of acoustic energy and provide electrical insulation. A central aperture 38 mm in diameter was provided for insertion of an imaging transducer. Figures 1(a)–(b) show the front and side views of the array and its holding mechanism that provided adjustment

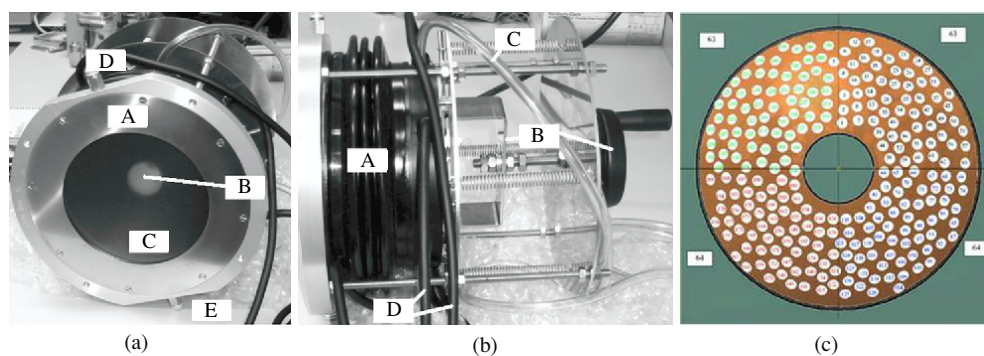


**Figure 1.** (a) Front view of the array and positioning mechanism: (A) stainless steel ring used to hold and seal the thin membrane, (B) the central hole for locating the imaging transducer (not shown), (C) part of the spherical surface of the array, and (D) and (E) entry and exit ports for the circulating temperature controlled, degassed water bolus. (b) (A) Flexible housing containing the water bolus, (B) screw mechanism for adjusting the position of the array with respect to the front membrane, (C) protective tube containing thermocouples for monitoring the array's temperature and (D) two of the four bundles of cables supplying RF signals to the four quadrants of elements. (c) The distribution of elements and their grouping into four quadrants containing (clockwise from top right) 63, 64, 64 and 63 elements, respectively. The outer diameter is 170 mm and the diameter of the central aperture is 38 mm.

of the position of the array relative to the thin membrane and therefore to the medium to be sonicated. The array could be operated within the frequency range 0.8 to 1.2 MHz. Data provided by the manufacturer showed that the efficiency varied by less than 3% from 0.8 to 1.1 MHz and fell approximately 4% from 1.1 to 1.2 MHz. In the testing described here an operating frequency of 1 MHz was used. RF signals were fed via four bundles of miniature coaxial cables to four groups of elements located in different quadrants of the surface of the array (figure 1(c)). The specified maximum acoustic power that could be delivered by each element was approximately 2.3 W. Provision for air cooling of the array was incorporated in the design and its internal temperature could be monitored by thermocouples. A flexible housing contained a temperature controlled degassed water bolus that was circulated using a pump and thermostatically controlled water bath (model GD120, Grant Instruments, Cambridge, UK).

## 2.2. RF power/control system

Generation and control of RF signals applied to the array elements were provided by a commercially available system (Model 500-013, Advanced Surgical Systems Inc., Tucson, AZ). The 256-channel system had a power capability of up to 60 W/channel, constrained within a total power of 1800 W and frequency was adjustable from 0.8 to 1.25 MHz. Four RF outputs via multi-pin connectors (ITT/Cannon type DL 156) provided power to the four quadrants of the array. 256 customized L-C impedance matching networks were designed and constructed. Measurements made on a sample of 254 channels showed better than approximately  $-10$  dB return loss. No further optimization of impedance matching by individually tuning each of the 254 channels was carried out. The matching networks were constructed in four groups of 64 and inserted between the four outputs of the generator and the quadrants of the array.

The generator was controlled by a laptop computer (Dell Latitude, Intel<sup>®</sup> Core<sup>™</sup> 2 Duo U7600 1.2 GHz processor, 2 GB RAM) via an RS-232 link. Proprietary software (Large Array Interface v1.2.0.0, Advanced Surgical Systems Inc., Tucson, AZ) was used to set the operating frequency and to select active channels and their relative phases (0 to 360° in increments of 2.25°) and relative powers (8 bit control) via a text file. The nominal electrical power level, limits on forward and reflected power per channel, and the duration of sonication were set via the main window of the user interface. The array could also be driven with a stack of files containing differing relative phases and powers. The rate at which this stack was sequenced and the relative power applied to each set of driving parameters within the stack could also be selected, or for refresh rates greater than 9 Hz, could be controlled by an external timing signal. Phase and power data for each of the 254 channels to produce and steer a single focus and patterns of multiple simultaneous foci were generated using a Fortran 90 code based on theory outlined below in section 2.4.2 and described in full by Gavrilov and Hand (2000a).

### 2.3. Ultrasound power measurements

Ultrasound power was determined using radiation force measurements with a target containing castor oil (Shaw 2008). The array and its holding system, pointed vertically, were fixed to a frame which also supported a water tank mounted above the array. The oil-filled target was placed in the tank and was suspended from a balance and positioned to intercept the whole of the ultrasound field generated by the array. A series of experiments were performed in which the array was driven on for 6.5 s and off for 6.5 s and when on, the power was stepped from 20% to 100% of the maximum power level set in steps of 20%. The output of the balance was recorded at 100 ms intervals throughout each experiment. The maximum electrical power applied to the array in these experiments was approximately 490 W.

### 2.4. Assessment of ultrasound intensity distributions in water

**2.4.1. Experimental assessment.** Since a method based on a scanned hydrophone would be prohibitively slow given the potentially large number of focusing conditions and fields that can be generated by the array, an alternative technique based on measurements made by using an infrared (IR) camera was used to provide a rapid qualitative assessment of field distributions, including identification of the existence and location of sidelobes and other local regions of high intensity. The method is based on imaging the temperature distribution produced in a thin absorbing layer by a short (0.1–0.2 s) burst of relatively low power (a few watts) ultrasound. In this case, it is possible to assume that the rate of change of temperature is proportional to intensity in a monofrequency field, and so the temperature distribution after a sufficiently short time should also be proportional to intensity. For simplicity of comparing theoretical and experimental results, the term intensity is often used in this paper but it should be recognized that, for the experimental results, this term is essentially a surrogate for the change in local temperature on the visible surface of the absorbing target.

The experimental setup is shown in figure 2. IR measurements were carried out using a modified ThermoScope<sup>®</sup> pulsed thermography system (Thermal Wave Imaging Inc., Ferndale, MI) consisting of an IR camera and a PC running EchoTherm<sup>®</sup> v6.4 software (Thermal Wave Imaging Inc., Ferndale, MI). The camera was a Phoenix MWIR 9705 (FLIR Systems, Boston, MA) operating in the band 1.5 to 5.0  $\mu\text{m}$  with a 14 bit indium antimonide detector providing 320  $\times$  256 pixels at a pitch of 30  $\mu\text{m}$ . Image data were transferred via an RS422 link to the PC. The system and software provided a method of acquiring, viewing and saving IR images synchronized to a pulsed source. The system was configured to capture a sequence of frames

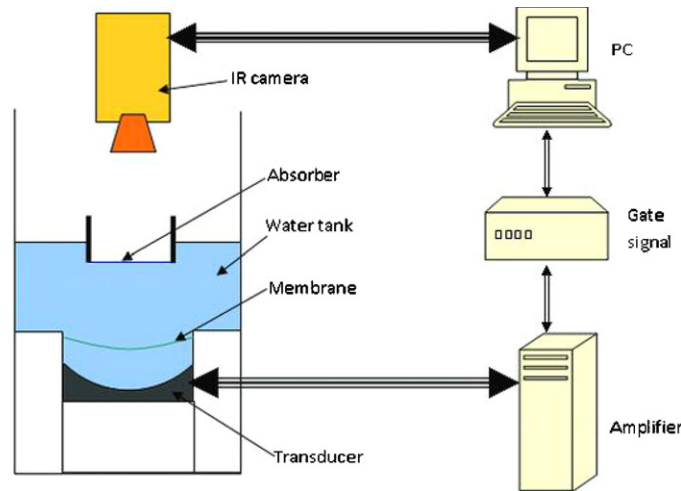


**Figure 2.** IR camera and absorber setup for assessment of intensity distributions produced by the array.

at a rate of 50 fps, with the ultrasound burst starting at the tenth frame, that was stored as a movie in RAW format to preserve the maximum dynamic range for later analysis. The distributions shown were of temperature change over a period of 0.08 s and were derived from the subtraction of the 10th frame from the 14th. The ultrasound beam was directed vertically upwards onto a 2.5 mm thick sheet of NPL F28 ultrasonic absorber (Precision Acoustics, Dorchester, UK) with a single-pass insertion loss of 7.5 dB at 1 MHz. The distance between the absorber and the transducer was adjustable using a micrometer positioning stage with  $\pm 25$  mm of travel. The other side of the sheet was air-backed and viewed from above by the IR camera which was focused on the upper surface of the sheet. The distance between the lens and the sheet was approximately 24 cm, giving a spatial resolution of 0.28 mm using a 25 mm lens. The thermal resolution was approximately 5.6 mK. The plane of the geometric focus of the array was determined by driving all elements with the same phase, and identifying the position of the micrometer where the maximum temperature rise was observed. This was determined at the start of each set of experiments and used as a datum. For the majority of measurements made, the nominal RF power supplied to the array was  $\leq 20$  W.

**2.4.2. Theoretically predicted distributions.** Intensity distributions for the patterns of single and simultaneous multiple foci measured experimentally were compared with those predicted theoretically using a method similar to that described by Goss *et al* (1996). The complex pressure distribution associated with a single plane circular element was found using the point radiator method in which the acoustic piston source was represented by many point radiators (Ocheltree and Frizzell 1989). Square elemental radiators of side length 0.1–0.25 mm were used to describe the radiating surface of each element 7 mm in diameter. Assuming radial symmetry for a circular element, its three-dimensional acoustic field was found by calculating the complex pressure  $p(r_s, z_s)$  as a function of the axial distance from the element,  $z_s$ , and the distance off its central axis,  $r_s$ , according to

$$p(r_s, z_s) = \frac{j\rho c k u_o \Delta A}{2\pi} \sum_{\text{surface}} \frac{e^{-(\alpha+jk)R}}{R}, \quad (1)$$

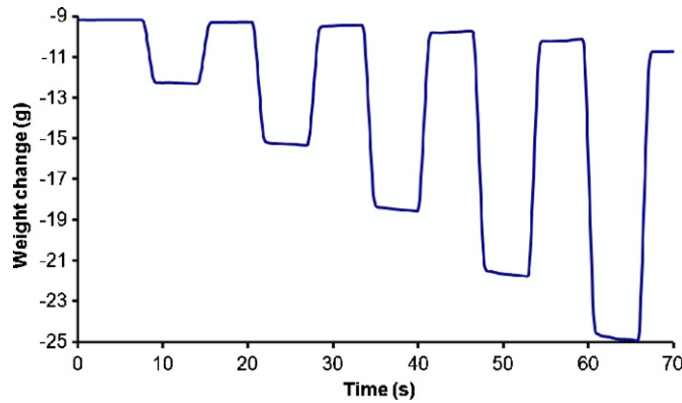


**Figure 3.** Changes in weight recorded by balance due to sonication for 6.5 s on and 6.5 s off as a function of time during which net electrical power applied is stepped from 98 W, through 196, 294 and 392 to 490 W with 50% duty cycle (6.5 s on, 6.5 s off).

where  $\rho$  is the density ( $1000 \text{ kg m}^{-3}$ ),  $c$  is the speed of sound ( $1500 \text{ m s}^{-1}$ ),  $k$  is the propagation constant,  $u_o$  is the velocity amplitude of the surface of the elemental sources,  $\Delta A$  is the area of each elemental source,  $\alpha$  is the attenuation coefficient (approximated to  $0 \text{ dB MHz}^{-1} \text{ cm}^{-1}$  for water) and  $R$  is the distance from the centre of an elemental source to the point  $(r_s, z_s)$  where the field is calculated. Complex pressure values were calculated at points on a  $0.1 \text{ mm}$  grid. The total complex pressure distributions from the 254 elements on the spherical shell were calculated by summing the complex pressure contributions from each element in the array at each point in the three-dimensional volume of interest as described by Gavrilov and Hand (2000a).

The relative phases of the velocities at the elements' surfaces required to produce a single focus were determined from the paths between the centre of each element and the position of the focus. To produce simultaneous multiple foci, the complex surface velocity  $u_n$  at the  $n$ th of the 254 elements was determined using the method described by Ebbini and Cain (1991). The  $u_n$  are related to the complex pressures  $p_m$  at each of  $M$  target points by the matrix equation

$$\mathbf{u} = \mathbf{H}^{*t} (\mathbf{H} \mathbf{H}^{*t})^{-1} \mathbf{p}, \quad (2)$$

where  $\mathbf{u} = [u_1, u_2, \dots, u_n, \dots, u_{254}]^t$ ,  $\mathbf{p} = [p_1, p_2, \dots, p_m, \dots, p_M]^t$  and  $\mathbf{H}$  is the  $M \times 254$  matrix with elements  $h_{mn} = \frac{j\rho ck}{2\pi} \int_S \frac{\exp(-jkr_{mn})}{r_{mn}} dS$ , where  $r_{mn}$  is the distance from the  $m$ th target point to the centre of the  $n$ th element and  $S$  is the area of an array element.  $\mathbf{H}^{*t}$  is the conjugate transpose of  $\mathbf{H}$  and  $[\ ]^t$  denotes transpose. To determine the  $u_n$  ( $n = 1, 2, \dots, 254$ ), equal amplitudes were assumed for the  $p_m$  ( $m = 1, 2, \dots, M$ ) and their phases were chosen such that the phases at the location of each maximum in the pattern of foci varied in a manner similar to that described by Fan and Hynynen (1996). The intensity at each grid point was found from the product of the complex pressure and its complex conjugate. Calculations were made using a FORTRAN 90 code and executed on a PC running Fortran PowerStation 4.0 in Microsoft Developer Studio (Filonenko *et al* 2004).

### 2.5. Sonication of pork meat

Several experiments were carried out to produce thermal ablation in various pieces of pork (pork chops, leg of pork). Typically, meat was degassed under vacuum for approximately 1 h

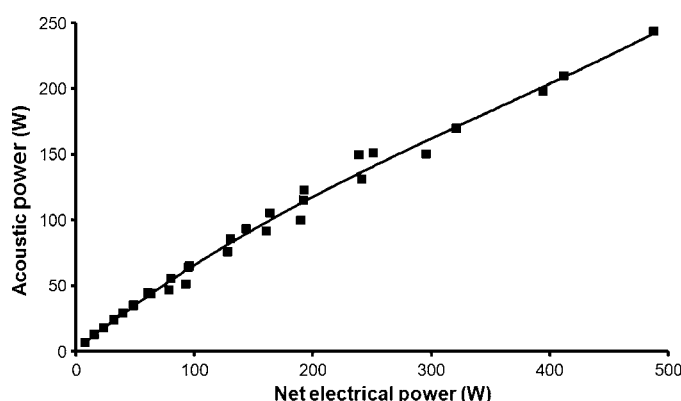


**Figure 4.** Acoustic power produced by the array, corrected for orientation of elements on the spherical surface, versus net electrical power applied.

prior to sonication. The oxygen level in the degassed water in the experimental tank and bolus was measured to be 0.85 ppm. To avoid contaminating this water, meat samples were trimmed to fit within a perspex cylinder with a base formed from a thin ( $\sim 10 \mu\text{m}$ ) cling-film membrane and placed on an annular spacer at the bottom of the container to avoid direct contact with the membrane. In some cases a small piece of liquid crystal film was placed on top of the assembly to identify the location of heating. The container and two meat stacked samples were positioned so that the common surfaces of the two samples were located approximately in the focal plane of the array.

### 3. Results

#### 3.1. Ultrasound power measurements

The output of the balance was recorded at 100 ms intervals throughout each experiment. Figure 3 shows a typical response of the balance during a period in which the array was turned on for 6.5 s and off for 6.5 s with various drive levels up to 490 W (net) electrical power. The absorbed ultrasound produced an instantaneous radiation force and a progressive heating of the castor oil. For a plane wave, the observed change in weight of the target  $\delta m$  is related to the acoustic power  $P$  through  $P = c\delta mg$ , where  $c$  is the speed of sound in the castor oil and  $g$  is the acceleration due to gravity. A correction factor was applied ( $P_{\text{corrected}} = 1.17 \times P_{\text{measured}}$ ) to account for the convergence of the acoustic field due to the distribution of elements on the spherical surface of the array.

Figure 4 shows the variation of acoustic power produced by the array with net electrical power applied. The efficiency of the array was  $\sim 73\%$  at low power levels, decreasing to  $\sim 50\%$  at high power levels. When the acoustic power was 244 W, the average power density at each of the 254 elements was  $\sim 2.5 \text{ W cm}^{-2}$ . Under these conditions a very approximate estimate of the predicted maximum intensity in a single focus on axis at the centre of curvature of the array, assuming linear propagation, is  $\sim 5.5 \text{ kW cm}^{-2}$  and the corresponding maximum pressure amplitude is  $\sim 13.2 \text{ MPa}$ . These estimates should be interpreted loosely since inevitably nonlinear effects will be present at such values of pressure and intensity.

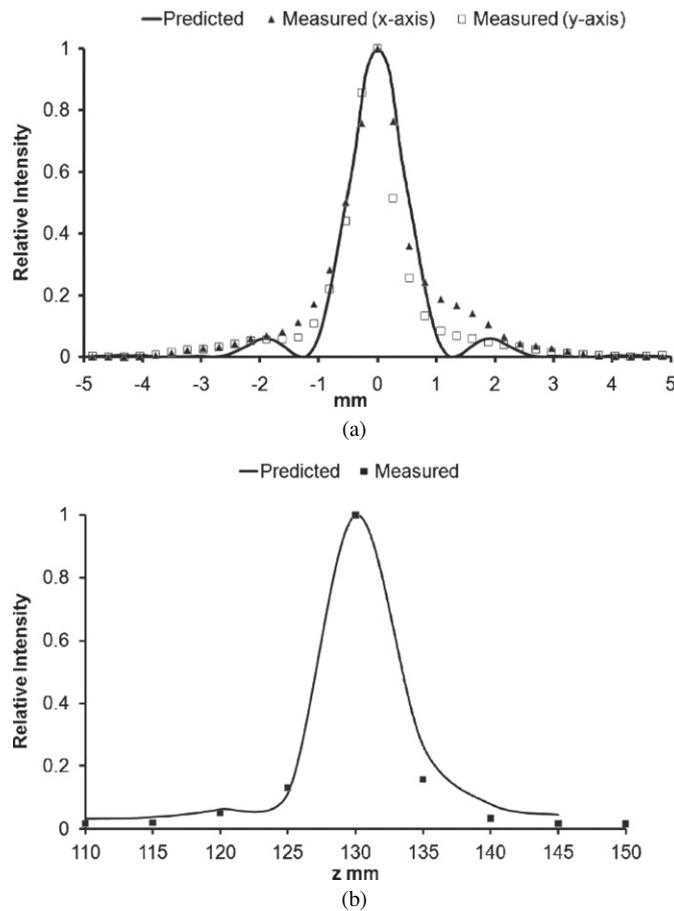


**Figure 5.** Relative intensity profiles for a single focus at  $(x, y, z) = (0, 0, 130)$ : (a) predicted (solid line) profiles along the  $x$ - and  $y$ -axes and corresponding measurements ( $\blacktriangle$ ,  $\square$ ) of temperature change, assumed to be a surrogate for intensity; (b) measured variation in maximum temperature change ( $\blacksquare$ ) and predicted (solid line) maximum intensity along the central axis of the array.

### 3.2. Ultrasound intensity distributions in water

During evaluation of the field distributions, the electrical input power was typically restricted to a low value of 20 W to minimize nonlinear propagation effects and allow comparison with theoretical estimates. For a given electrical power, the peak pressure and intensity in the focal region depends on the number of simultaneous foci and the amount of beam-steering applied: for 20 W electrical power, the acoustic power produced was 14.6 W and the average intensity at each of the 254 elements was  $\sim 0.15 \text{ W cm}^{-2}$ . Under these conditions a very approximate estimate of the predicted maximum intensity in a single focus on axis at the centre of curvature of the array, assuming linear propagation, is  $\sim 0.33 \text{ kW cm}^{-2}$  and the corresponding maximum pressure amplitude is  $\sim 3.2 \text{ MPa}$ .

#### 3.2.1. Single focus

*Single focus located on axis at the centre of curvature.* The measured  $-6 \text{ dB}$  full width of a single focus targeted at the centre of curvature of the array (i.e. at coordinates  $(x, y, z) =$

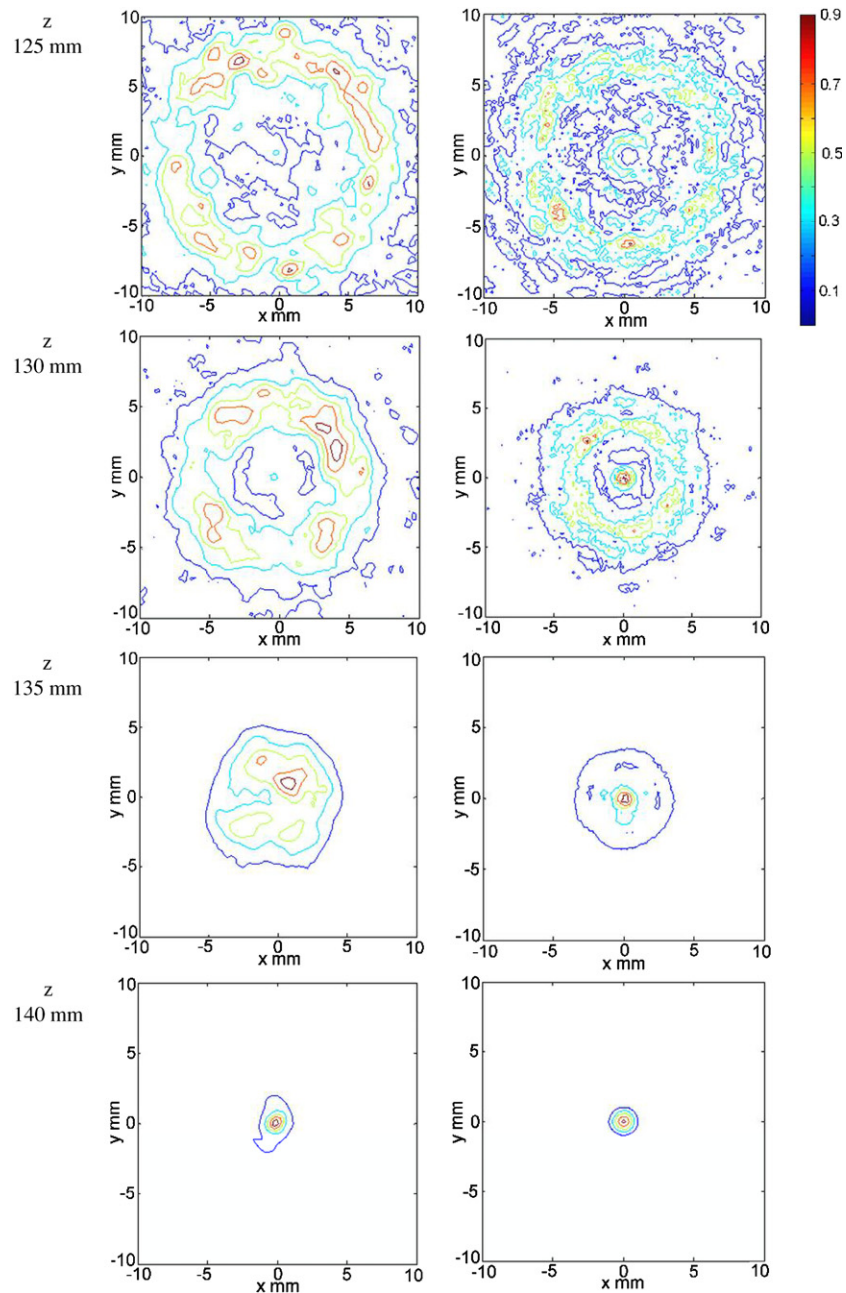


**Figure 6.** Measured (left column) and predicted (right column) distributions in  $x$ - $y$  planes at  $z = 125, 130, 135$  and  $140$  mm for a single focus on axis and focused at  $z = 140$  mm. In each case, contours are normalized to the maximum for that distribution.

$(0, 0, 130)$  was  $1.6$  mm, compared to the predicted value of  $1.7$  mm, as shown in figure 5(a). Figure 5(b) compares the variation in maximum intensity with axial distance obtained by the IR measurement of temperature changes and the predicted variation.

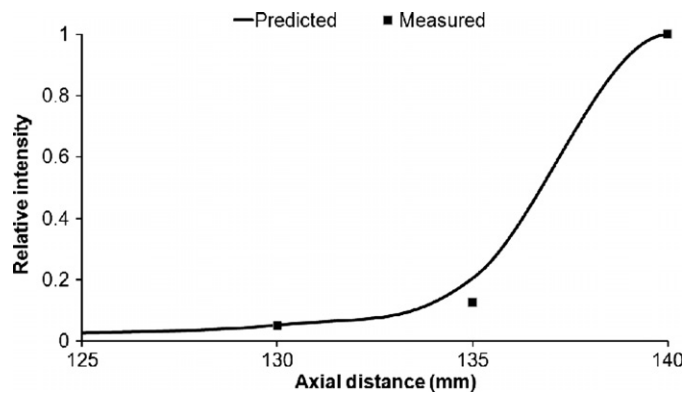


**Figure 7.** Dependence of measured change in temperature and predicted maximum intensity with axial distance over the range 125–140 mm. Normalization is to the respective maximum value in the plane  $z = 140$  mm.

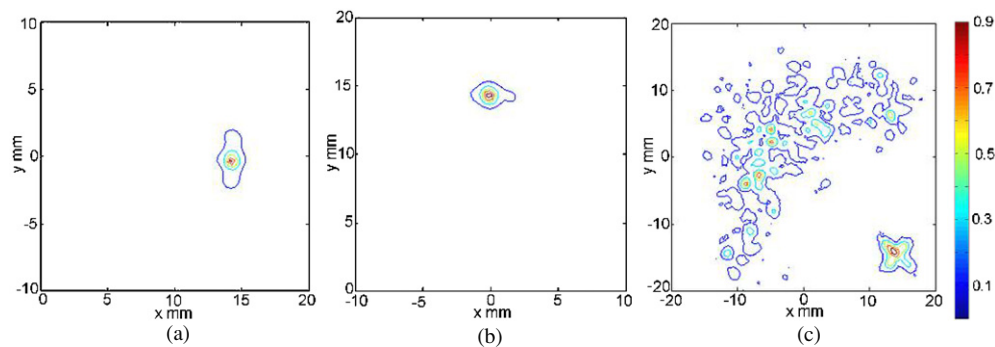


**Figure 8.** Measured distributions of temperature change for a single focus steered to (a)  $(x, y, z) = (15, 0, 130)$ ; (b)  $(x, y, z) = (0, 15, 130)$ ; and (c)  $(x, y, z) = (15, -15, 130)$ . Each distribution is normalized to its maximum value and contours are at 10, 30, 50, 70 and 90% of that maximum.

*Single focus located on axis out of the plane containing the centre of curvature.* Figure 6 shows measured and predicted distributions in  $x$ - $y$  planes at  $z = 125, 130, 135$  and  $140$  mm for a single focus on axis and focused at  $z = 140$  mm. The variation of maximum intensity with axial distance over the same range is shown in figure 7. The  $-6$  dB half length of the focal region was 4 mm. In the plane  $z = 140$  mm its  $-6$  dB full width was approximately 2 mm. When a single focus was targeted on axis at  $z = 120$  mm, the predicted  $-6$  dB full length and full width were 7.2 mm and 1.5 mm, respectively; these values were also in good agreement with measurements. Cases in which the focus was shifted axially up to  $\pm 20$  mm from the centre of curvature were also investigated and results showed that intensity away from the focal region was  $< -10$  dB relative to the maximum for shifts  $\Delta z$  for which  $15 \leq \Delta z < 20$  mm, in accord with linear theoretical predictions.

*Single focus steered off axis.* Figures 8(a) and (b) show IR measured temperature changes when a single focus was steered 15 mm along the array's  $x$ - and  $y$ -axes, respectively, in the

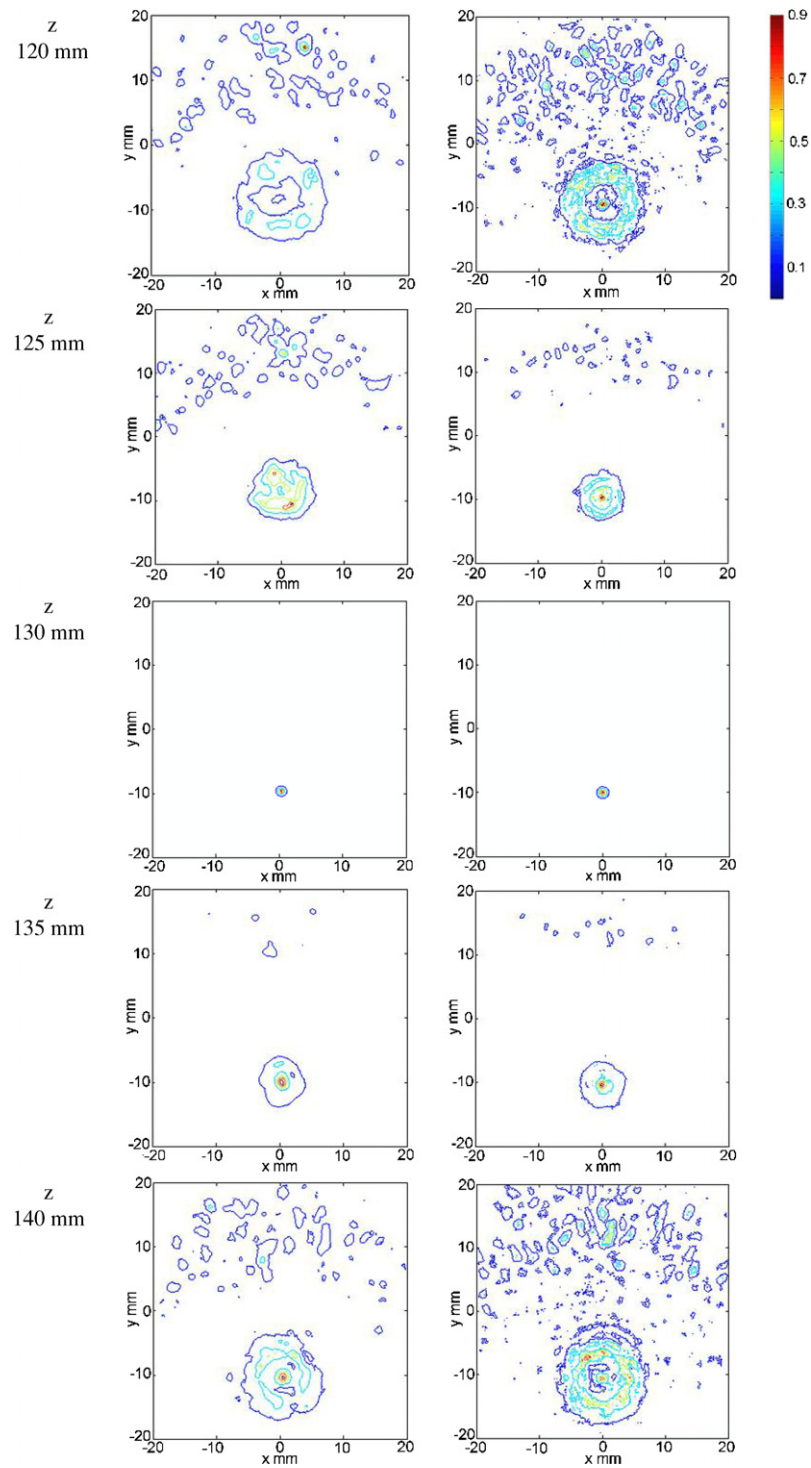


**Figure 9.** Measured temperature change (left column) and predicted intensity (right column) distributions in  $x$ - $y$  planes at  $z = 120, 125, 130, 135$  and  $140$  mm for a single focus located at  $(x, y, z) = (0, -10, 130)$ . Each case is normalized to its maximum value.

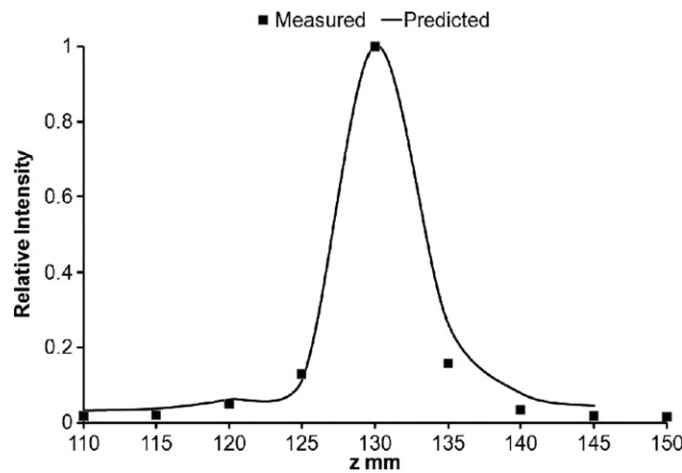


**Figure 10.** Dependence of measured temperature change and predicted maximum intensity with axial distance over the range 110–150 mm for a single focus located at  $(x, y, z) = (0, -10, 130)$ . Normalization is to the respective maximum value in the plane  $z = 130$  mm.

$z = 130$  mm plane. In each case the peak of the distribution is within 1 mm of the targeted position and temperature changes away from the immediate location of the focus are less than 10% of the maximum. However, as shown in figure 8(c), when the focus is steered 15 mm off both  $x$ - and  $y$ -axes (i.e. approximately 21 mm from the central axis) with  $z = 130$  mm, the observed distribution shows local ‘hot spots’ away from the targeted location in which the change is in excess of 70% of the maximum. IR measured temperature changes and predicted intensity distributions in  $x$ - $y$  planes from  $z = 120$  mm to 140 mm for a single focus steered to  $(0, -10, 130)$  are shown in figure 9. The maximum values in these planes plotted against axial distance for both predictions and measurements are shown in figure 10.

*Multiple simultaneous foci.* The phases at the 254 elements were calculated so as to produce patterns of four and five foci. In the case of the pattern consisting of four foci, the foci were targeted at  $(4, 0, 130)$ ,  $(0, -4, 130)$ ,  $(-4, 0, 130)$  and  $(0, 4, 130)$ . This case was referred to by the location of the centre of the pattern for which  $(x, y, z) = (0, 0, 130)$ . In the case of the pattern of five foci, when centred, these occurred at  $(x, y, z)$  values of  $(4, 4, 130)$ ,  $(4, -4, 130)$ ,  $(-4, -4, 130)$ ,  $(-4, 4, 130)$  and  $(0, 0, 130)$ . When the patterns were steered off axis and focused in different  $x$ - $y$  planes, the coordinate describing the position referred to the central point in the pattern.

*Patterns of four and five foci.* Figures 11(a)–(c) show measured distributions for the pattern of four simultaneous foci in the plane at  $z = 130$ , with the centre of the pattern located at  $(0, 0, 130)$ ,  $(0, 10, 130)$  and  $(0, 15, 130)$ , respectively. With the exception of the case when the pattern is steered to  $(x, y, z) = (0, 15, 130)$ , the secondary intensity maxima are below approximately 25% of the peak value. Figures 11(d)–(f) show measured distributions for the pattern of five simultaneous foci located at  $(0, 0, 130)$ ,  $(0, 10, 130)$  and  $(-10, 10, 130)$ , respectively. With the exception of the latter case, the secondary intensity maxima are again below approximately 25% of the peak value. Figures 11(g) and (h) show the results of switching between the patterns of four and five simultaneous foci when these are located at

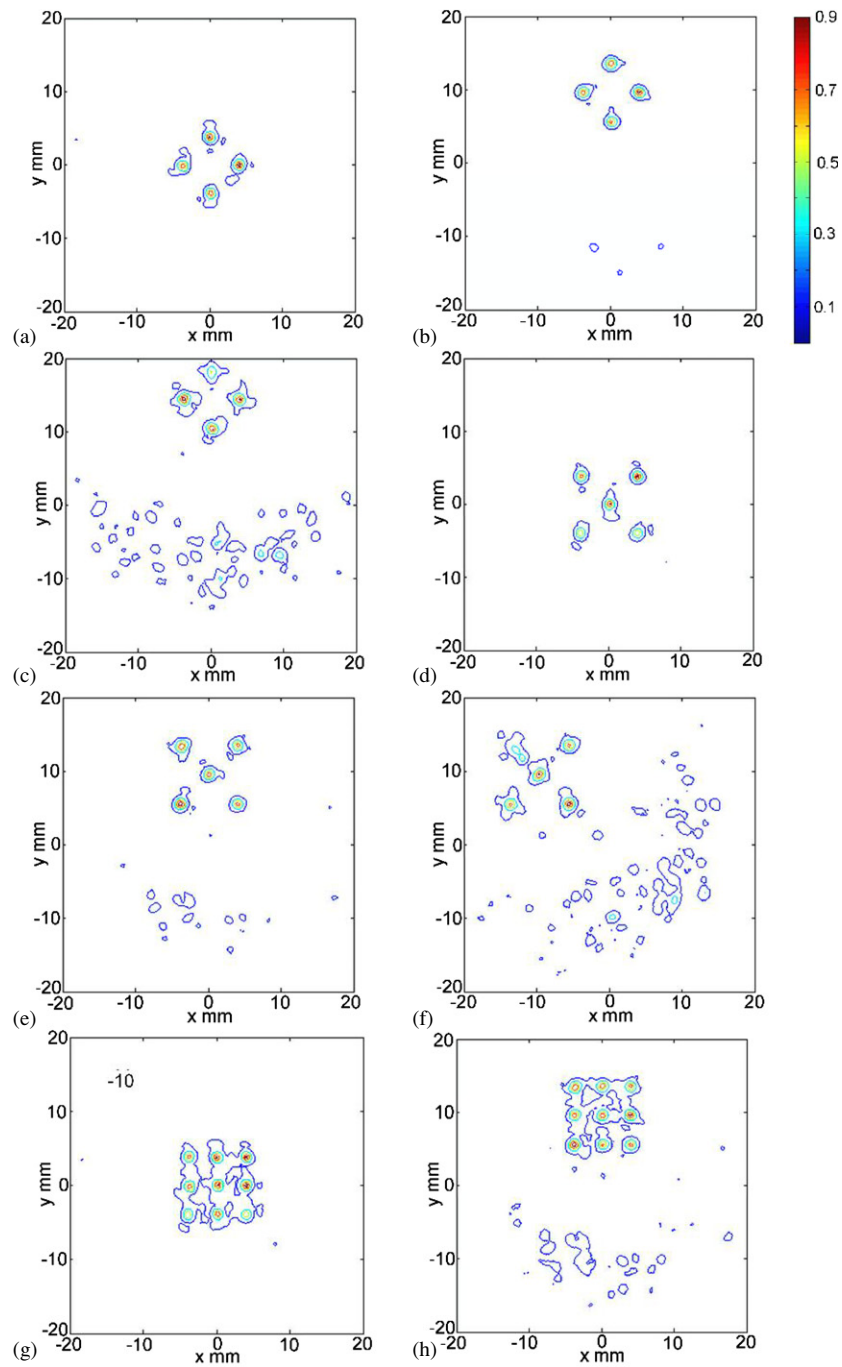


**Figure 11.** Measured temperature changes for multiple simultaneous foci in the plane  $z = 130$  mm on and steered off the central axis. Four foci at (a)  $(x, y, z) = (0, 0, 130)$ ; (b)  $(x, y, z) = (0, 10, 130)$ ; (c)  $(x, y, z) = (0, 15, 130)$ . Five foci at (d)  $(x, y, z) = (0, 0, 130)$ ; (e)  $(x, y, z) = (0, 10, 130)$ ; (f)  $(x, y, z) = (-10, 10, 130)$ . Results of switching between patterns of four and five foci at (g)  $(x, y, z) = (0, 0, 130)$  and (h)  $(x, y, z) = (0, 10, 130)$ . In all distributions, contours are at 10, 30, 50, 70 and 90% of the maximum value in each case.

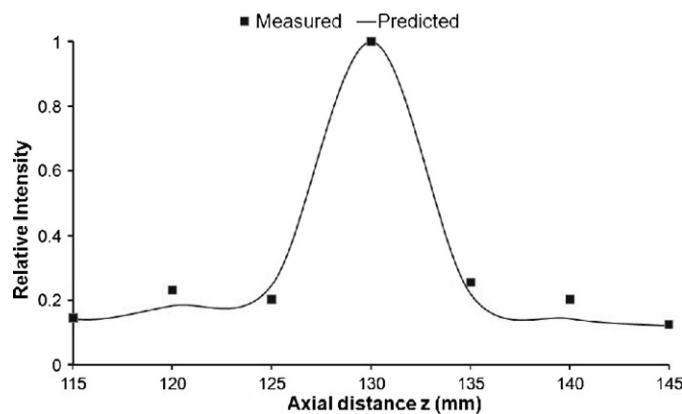


**Figure 12.** Relative maxima in  $z$  planes for predicted intensity and measured temperature change data versus axial distance  $z$  for the case of the pattern of four foci located at  $(x, y, z) = (0, 10, 130)$ .

$(0, 0, 130)$  and  $(0, 10, 130)$ , respectively. Although the multiple foci in these examples were intended to have equal peak values (and assumed equal power delivery from all elements), the measurements show some variation between foci. This could be due to the limited spatial resolution of  $\sim 0.28$  mm in the configuration used or because some elements provided more acoustic power than others. Figure 12 shows relative intensity maxima in  $z$  planes for predicted and measured data *versus* axial distance  $z$  for the case of the pattern of four foci located at  $(x, y, z) = (0, 10, 130)$ . It was also possible to steer patterns of four and five foci up to 10 mm off axis at distances between 125 mm and 140 mm with acceptable sidelobe levels.

### 3.3. Sonication of pork meat

Sonication of pork samples was carried out at room temperature. Single focus lesions were produced as listed in table 1. Sonications were performed at approximately 10 min intervals to avoid thermal buildup within the tissue. Figure 13 shows some details of the resulting lesions. The length of lesion 1 (4 mm) was unexpectedly smaller than those observed for lesions 2 and 3 and may have been inaccurate due to the difficulty in measuring some of the lesions. Caliper measurements showed that the distance between lesions 2 and 3 was 18.5 mm compared with the intended separation of 20 mm, and these were equidistant from lesion 1. Increasing the electrical power applied to the array by approximately a factor of 2 (lesion 4 compared with lesion 1) but maintaining an exposure duration of 20 s resulted in a modest increase in length (compared with lesions 2 and 3) but an increase of two to three times in diameter. In the cases of lesions 4 and 5, increasing the duration of exposure by a factor of 2 produced a lesion of twice the length and with 50% increase in the diameter.

To show the ability to produce multiple-foci lesions, patterns of four simultaneous foci (individual foci in the pattern targeted at  $(4, 0, 130)$ ,  $(0, 4, 130)$ ,  $(-4, 0, 130)$  and  $(0, -4, 130)$ ) followed by five simultaneous foci (individual foci at  $(4, 4, 130)$ ,  $(-4, 4, 130)$ ,  $(-4, -4, 130)$ ,  $(4, -4, 130)$  and  $(0, 0, 130)$ ) were produced. The approximate acoustic power emitted by the array was 142 W for the pattern of four foci and 188 W for the pattern of five foci. In each case the duration of exposure was 20 s. Upon the inspection of the meat samples a large contiguous lesion with lateral dimensions approximately  $11 \text{ mm} \times 11 \text{ mm} \times 16 \text{ mm}$  was observed. Serial sections (approximately normal to the direction of ultrasound propagation)

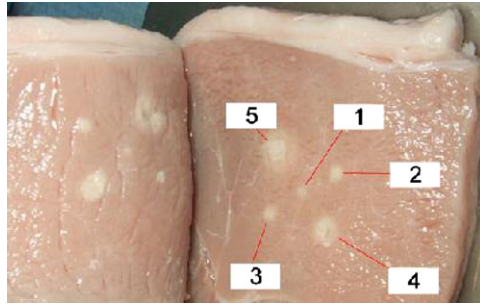


**Figure 13.** Single focus lesions (see table 1) produced in pork: overview showing lesions 2, 1 and 3 (diagonally from upper right to lower left on the right-hand sample), lesion 4 (lower right on the right-hand sample) and lesion 5 (upper left on the right-hand sample) on mid-surfaces of the meat samples

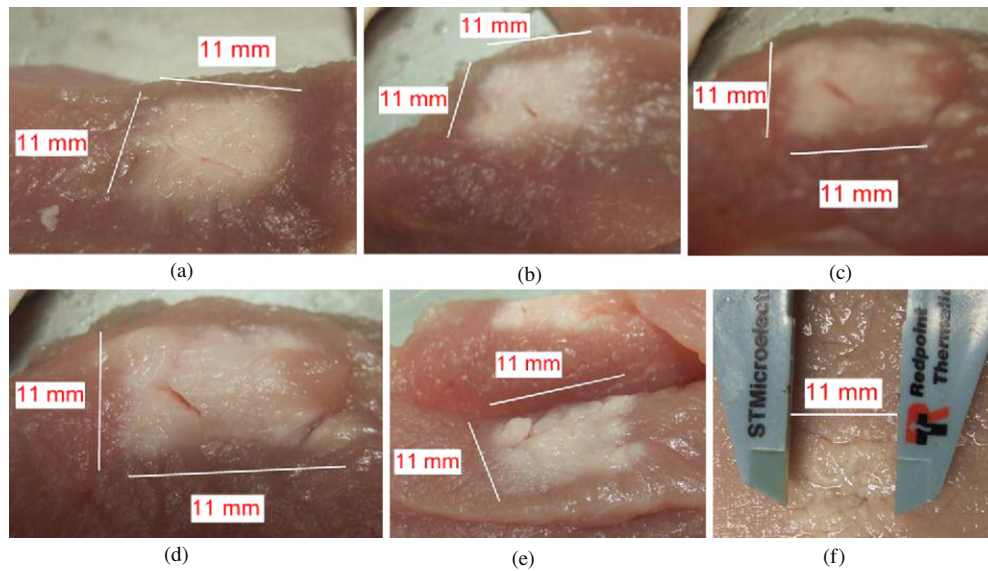


**Figure 14.** Lesion produced by a sequence of four foci (142 W acoustic power, 20 s) followed by five foci (188 W acoustic power, 20 s). (a)–(e) Sequential sections through lesion showing essentially square cross sections. The sections covered approximately 16 mm of tissue; (f) lesion (11 mm side length).

are shown in figure 14. A similar experiment with the same power levels but with an increased exposure duration (30 s) produced a single contiguous lesion approximately 16 mm  $\times$  14 mm and of length 27 mm (at edge) and 28 mm (central region).

The ability to steer multiple foci off axis in tissue was demonstrated using a sequence of five foci on axis (0, 0, 130) followed by four foci steered 10 mm off axis (10, 0, 130) with acoustic power of 187 W and 152 W, respectively, delivered to the array and a duration of 25 s in each case. The resulting lesion is shown in figure 15.

The ability to steer single and multiple foci along the central axis was demonstrated by an experiment in which a single focus lesion (54 W acoustic power for 30 s) was targeted at

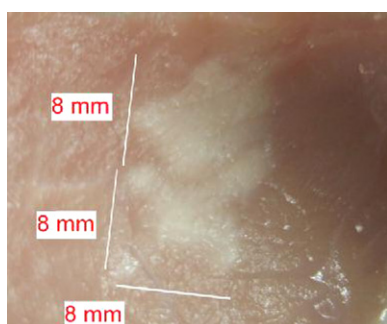


**Figure 15.** Lesion produced by a sequence of five foci (187 W acoustic power, 25 s) followed by four foci offset by 10 mm (152 W acoustic power, 25 s). The ‘cross’ and ‘diamond’ due to the patterns of five and four foci, respectively, are evident in this section.

**Table 1.** Details of five single focus lesions produced in pork meat (see figure 13).

Lesion	Acoustic power (W)	Time (s)	Length (mm)	Width (mm)
1	59	20	4	2
2	80	20	8.5	3
3	80	20	7.5	3
4	115	20	10.1	6.3
5	115	40	21	9

(0, 0, 140), a second single focus lesion (59 W acoustic power for 30 s) was targeted at (0, 0, 130) and a pattern of five foci (189 W acoustic power for 20 s) was targeted at (0, 0, 120). Figure 16 shows some details of the resulting lesions. Square and single lesions were detected at differing depths in the tissue. All three exposures produced a lesion on the axis; a section showing part of a contiguous lesion over a thickness of 33 mm of tissue resulting from these axial lesions can be seen.

#### 4. Discussion

Previous work (Gavrilov and Hand 2000a, 2000b, Gavrilov *et al* 2000) has shown that improvement of the quality of the intensity distributions, particularly in cases when the focus or foci is/are steered from the geometric centre of curvature of the array, can be achieved if three conditions are fulfilled simultaneously. These are (i) the elements should be randomly distributed over the array surface, (ii) element dimensions should be comparable to one or a few ultrasound wavelengths and (iii) the active surface of the array should be large enough to ensure a sufficiently high intensity in the focus whilst avoiding excessively tight packing of the elements. The good agreement between measurements and predictions discussed in this paper supports these design criteria. The benefits of using arrays in which the locations of the elements are randomized have been recognized for many years and this approach has been applied to diverse problems (Skolnik 1962, Turnbull and Foster 1991), as well as to therapeutic ultrasound systems (Goss *et al* 1996). Recent reports involving therapeutic applications of randomized arrays include those by Pernot *et al* (2003), Aitkenhead *et al* (2008) and Aubry *et al* (2008).

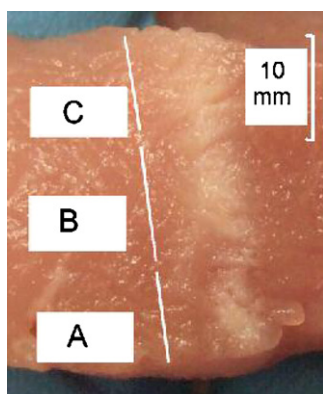


**Figure 16.** Section through tissue showing an essentially contiguous lesion along the central axis due to a sequence of single focus lesions at  $(0, 0, 140)$ ,  $(0, 0, 130)$  and  $(0, 0, 120)$ . 'A' is due to the single focus at  $(0, 0, 140)$ , 'B' due to that at  $(0, 0, 130)$  and 'C' due to that at  $(0, 0, 120)$ . Ultrasound propagated from top to bottom through this section of tissue.

The potential benefit of the use of a phased array to produce relatively large volumes of thermally ablated tissue has been described by several authors. Daum and Hynynen (1999) investigated switching between various patterns of multiple foci. Filonenko *et al* (2004) studied thermal dose distributions associated with a regime of nine foci produced by a random phased array, including cases where the patterns were steered up to 7 mm off axis. Alternatively, scanning a focus along spiral and other trajectories (Mougenot *et al* 2004, Malinen *et al* 2005) has also been shown to be effective in producing large thermal lesions. Other potential advantages of extracorporeal phased arrays include the possibility of customizing the acoustic field to enable ablation of liver by sonicating through intercostal spaces and without overheating the ribs (McGough *et al* 1996, Botros *et al* 1997, 1998, Aubry *et al* 2008). Preliminary investigations using the current phased array for this purpose have been carried out and will be the subject of a future publication.

To our knowledge, the use of an IR camera to map intensity distributions in the way described is new. It is very useful in that a 2D field map can be generated within seconds, although it necessitates the introduction of an air interface and acoustic reflections into the beam path. The measured distribution is also, of course, dependent on thermal conduction and convection, and on the spectral content of the acoustic field. Conduction and convection effects have been minimized by using only sub-second exposure periods; we found that the temperature increase was a linear function of time for the first 0.2 s, indicating that these effects are small over the time scale considered. Acoustic reflections are reduced by the high attenuation coefficient of the F28 rubber used as the window material for which the two-way insertion loss is approximately 15 dB. Reflections can be a problem for characterizing unfocused transducers, but much less so in the focal region of a focused transducer. Here, the intensity level of the main incident beam is much higher than the levels from the first reflection (which has to travel three times the distance) and so the pattern is dominated by the main beam. Enhanced temperature rise in regions of the field containing nonlinear harmonics can be expected; however, these evaluations were carried out at low drive levels to minimize nonlinear propagation effects and, if present, these harmonics will be more highly attenuated by the window material and so their influence on the outer surface may be limited.

The pork meat experiments were carried out over relatively long durations for a single HIFU exposure (up to 30 s) but the ablated volume was large for the multiple focus fields, which inevitably requires more energy to be delivered. We have not tried to identify the minimum time required to produce a single small lesion. It is also worth noting that the experiments were carried out at room temperature, thus requiring a temperature increase of approximately 40 °C to achieve ablation. Starting from body temperature, the increase (and therefore time) required will be greatly reduced, especially where ablation is achieved between individual focal points by thermal conduction.

## 5. Conclusion

Laboratory testing of a random phased array HIFU device and associated electronics has shown that the position of the focus or a pattern of simultaneous multiple foci can be controlled dynamically, and that steering of single and multiple foci in depth and laterally from the central axis is possible whilst maintaining low intensity levels in secondary maxima away from the targeted area. These results are in good agreement with linear theoretical predictions. Experiments in which pork meat was thermally ablated indicate that single and multiple foci lesions can be steered off and along the central axis of the array. Large contiguous lesions can be produced using the patterns of multiple foci and relatively short exposure times.

## Acknowledgments

This work was supported by Cancer Research UK through project grant C18509/A78. J Hand is also grateful for support from the NIHR Biomedical Research Centre funding scheme. A Shaw, N Sadhoo and S Rajagopal were also supported in part by the National Measurement Systems Directorate of the UK Department of Innovation, Universities and Skills. L Gavrilov is grateful for support from the INTAS (project no 05-1000008-7841) and the Russian Foundation for Basic Research (project no 09-02-00066-a).

## References

- Aitkenhead A H, Mills J A and Wilson A J 2008 The design and characterization of an ultrasound phased array suitable for deep tissue hyperthermia *Ultrason. Med. Biol.* **34** 1793–807
- Aubry J-F, Pernot M, Marquet F, Tanter M and Fink M 2008 Transcostal high-intensity-focused ultrasound: *ex vivo* adaptive focusing feasibility study *Phys. Med. Biol.* **53** 2937–51
- Botros Y Y, Ebbini E S and Volakis J L 1998 Two-step hybrid virtual array-ray (VAR) technique for focusing through the rib cage *IEEE Trans. Ultrason. Ferroelectr. Freq. Control* **45** 989–99
- Botros Y Y, Volakis J L, VanBaren P and Ebbini E S 1997 A hybrid computational model for ultrasound phased-array heating in presence of strongly scattering obstacles *IEEE Trans. Biomed. Eng.* **44** 1039–50
- Daum D R and Hynynen K 1999 A 256-element ultrasonic phased array system for the treatment of large volumes of deep seated tissue *IEEE Trans. Ultrason. Ferroelectr. Freq. Control* **46** 1254–68
- Dubinsky T J, Cuevas C, Dighe M K, Kolokythas O and Hwang J H 2008 High-intensity focused ultrasound: current potential and oncologic applications *Am. J. Roentgenol.* **190** 191–9
- Dupenloup F, Chapelon J Y, Cathignol D J and Sapozhnikov O A 1996 Reduction of the grating lobes of annular arrays used in focused ultrasound surgery *IEEE Trans. Ultrason. Ferroelectr. Freq. Control* **43** 991–8
- Ebbini E S and Cain C A 1991 A spherical-section ultrasound phased-array applicator for deep localized hyperthermia *IEEE Trans. Biomed. Eng.* **38** 634–43
- Fan X and Hynynen K 1996 A study of various parameters of spherically curved phased arrays for non-invasive ultrasound surgery *Phys. Med. Biol.* **41** 591–608
- Filonenko E A, Gavrilov L R, Khokhlova V A and Hand J W 2004 Heating of biological tissues by two-dimensional phased arrays with random and regular element distributions *Acoust. Phys.* **50** 222–31

- Gavrilov L R and Hand J W 2000a A theoretical assessment of the relative performance of spherical phased arrays for ultrasound surgery *IEEE Trans. Ultrason. Ferroelectr. Freq. Control* **47** 125–39
- Gavrilov L R and Hand J W 2000b Two-dimensional phased arrays for surgery: movement of a single focus *Acoust. Phys.* **46** 390–9
- Gavrilov L R, Hand J W, Abel P and Cain C A 1997 A method of reducing grating lobes associated with an ultrasound linear phased array intended for transrectal thermotherapy *IEEE Trans. Ultrason. Ferroelectr. Freq. Control* **44** 1010–7
- Gavrilov L R, Hand J W and Yushina I G 2000 Two-dimensional phased arrays for application in surgery: scanning by several focuses *Acoust. Phys.* **46** 551–8
- Goss S A, Frizell L A, Kouzmanoff J T, Barich J M and Yang J M 1996 Sparse random ultrasound phased array for focal surgery *IEEE Trans. Ultrason. Ferroelectr. Freq. Control* **43** 1111–21
- Hand J W and Gavrilov L R 2000 Ultrasound transducer array *GB Patent* GB2347043 A
- Hand J W and Gavrilov L R 2002 Arrays of quasi-randomly distributed ultrasound transducers *US Patent* 6488630
- Hutchinson E B, Buchanan M T and Hynynen K 1996 Design and optimization of an aperiodic ultrasound phased array for intracavitary prostate thermal therapies *Med. Phys.* **23** 767–76
- Lu M, Wan M, Xu F, Wang X and Zhong H 2005 Focused beam control for ultrasound surgery with spherical-section phased array: sound field calculation and genetic optimization algorithm *IEEE Trans. Ultrason. Ferroelectr. Freq. Control* **52** 1270–90
- Malinen M, Huttunen T, Kaipio J P and Hynynen K 2005 Scanning path optimization for ultrasound surgery *Phys. Med. Biol.* **50** 3473–90
- McGough R J, Kessler M L, Ebbini E S and Cain C A 1996 Treatment planning for hyperthermia with ultrasound phased arrays *IEEE Trans. Ultrason. Ferroelectr. Freq. Control* **43** 1074–84
- Mougenot C, Salomir R, Palussiere J, Grenier N and Moonen C T 2004 Automatic spatial and temporal temperature control for MR-guided focused ultrasound using fast 3D MR thermometry and multispiral trajectory of the focal point *Magn. Reson. Med.* **52** 1005–15
- Ocheltree K and Frizzell L 1989 Sound field calculations for rectangular sources *IEEE Trans. Ultrason. Ferroelectr. Freq. Control* **36** 242–8
- Pernot M, Aubry J F, Tanter M, Thomas J L and Fink M 2003 High power transcranial beam steering for ultrasonic brain therapy *Phys. Med. Biol.* **48** 2577–89
- Shaw 2008 A buoyancy method for the measurement of total ultrasound power generated by HIFU transducers *Ultrasound Med. Biol.* **34** 1327–42
- Skolnik M I 1962 *Introduction to Radar Systems* (New York: McGraw-Hill)
- ter Haar G and Coussios C 2007 High intensity focused ultrasound: physical principles and devices *Int. J. Hyperth.* **23** 89–104
- Turnbull D H and Foster F S 1991 Beam steering with pulsed two-dimensional transducer arrays *IEEE Trans. Ultrason. Ferroelectr. Freq. Control* **38** 320–33